Sustainable Energy & Fuels

ROYAL SOCIETY OF CHEMISTRY

PAPER

View Article Online
View Journal | View Issue

Cite this: *Sustainable Energy Fuels*, 2025, **9**, 5004

A sustainable anode for Na-ion batteries based on holm oak waste-derived hard carbon and lignin binder

Luca Bottoni, *[a] Hamideh Darjazi, †[ab] Leonardo Sbrascini, [a] Antunes Staffolani, ‡[a] Genny Pastore,[a] Luca Minnetti, [ab] Federico Verdicchio, [ab] Serena Gabrielli, [a] Andrea Catorci[c] and Francesco Nobili [ab]

Sodium-ion batteries (SIBs) represent one of the key-enabling technologies for the ongoing energy transition. However, the economic success of SIBs relies on sustainable and low-cost electrode materials, such as the bio-derived ones. Particularly, it is important to find an environmentally friendly alternative to the commercial binder polyvinylidene fluoride, which currently poses several concerns in terms of environmental impact together with the other perfluorinated alkylated substances (PFAS). In this context, a holm oak waste biomass was used both for the production of hard carbon and as a source of lignin (a natural binder that is currently poorly valorized). A one-step pyrolysis of holm-oak waste followed by acid leaching was performed to obtain a hard carbon with low amount of impurities, good interlayer spacing and well-developed microporosity and surface area. On the other hand, lignin was extracted from holm oak waste feedstock through an organosolv process with a binary mixture of γ-valerolactone and water, obtaining a lignin with a high level of purity. The obtained materials were combined to prepare bio-based anode materials for SIBs, exhibiting a reversible capacity of around 200 mA h g^{-1} in Na half-cells cycled at 300 mA g^{-1}, with promising rate capability and long cycling stability even at high current rates. The electrochemical results combined with the interfacial and post-mortem SEM analysis demonstrated the ability of lignin binder to ensure longstanding adhesion with the hard carbon substrate, reflecting in electrodes with long cycle life and capacity retention.

Received 6th May 2025
Accepted 18th July 2025

DOI: 10.1039/d5se00645g

rsc.li/sustainable-energy

1 Introduction

Currently, lithium-ion batteries (LIBs) represent the most used energy storage technology for a wide range of applications owing to their relatively high energy (up to 260 Wh kg^{-1})[1] and power densities (600–3000 W kg^{-1}), high round-trip efficiency, long cycle life (500–10000 cycles) and low self-discharge (around 1–5% per month).[2] However, the huge increase in the demand for LIBs, mainly driven by the electrified vehicle market,[3] is posing serious concerns about the future availability of the so-called "Critical Raw Materials" defined by the European Commission, which includes common elements necessary for lithium-ion batteries, such as lithium, cobalt, nickel, natural graphite and fluorine.[4] In this context, sodium-ion batteries (SIBs) represent a promising alternative to LIBs; they are particularly appealing for large-scale stationary energy storage[5,6] mainly because of the 1000-time higher abundance of Na resources than Li and wider global distribution,[7] which result in lower cost of Na-containing raw materials (0.19 \$ kg^{-1} for Na_2CO_3 *vs.* 10.49 \$ kg^{-1} for Li_2CO_3 in February 2025).[8] Other key advantages of SIBs are the lower reliance on critical raw materials such as those mentioned above and the possibility of using aluminum current collectors for both cathode and anode electrodes. This is beneficial for the decrease in cost and weight, and the possibility of storage at a fully discharged state makes handling and transportation safer.[9] All these aspects, coupled with sustainable manufacturing processes, result in low costs for SIBs, offering large opportunities for their penetration into the LIB market, especially for stationary energy storage. Despite LIBs and SIBs sharing the same "rocking chair" working principle, there are some differences between these systems, which imply that materials used in LIBs cannot be straightforwardly transferred to the SIB counterpart. This is the case for graphite,

[a]*School of Science and Technology, Chemistry Division, University of Camerino, Via Madonna delle Carceri snc, Camerino, Italy. E-mail: luca.bottoni@unicam.it*

[b]*GISEL – Centro di Riferimento Nazionale per i Sistemi di Accumulo Elettrochimico di Energia, INSTM, Via Giuseppe Giusti 9, Firenze, Italy*

[c]*School of Biosciences and Veterinary Medicine, University of Camerino, Via Pontoni 5, Camerino, Italy*

† Current Affiliation: Group of Applied Materials and Electrochemistry – GAME Lab, Department of Applied Science and Technology – DISAT, Politecnico di Torino, Corso Duca degli Abruzzi 24, Torino, Italy.

‡ Current Affiliation: Department of Chemistry "Giacomo Ciamician", University of Bologna, Via Francesco Selmi 2, Bologna, Italy.

the state-of-the-art anode material for LIBs, which exhibits poor performance in sodium-ion systems, mostly because of thermodynamic limitations for Na intercalation into graphite.[10] More interesting results have been obtained using non-graphitizable carbons, known as hard carbons (HCs), which are currently the "first-generation" active materials at the anode side for SIBs.[11] HCs are characterized by disordered and incoherent structures, resulting in a sodium storage mechanism that is not yet completely elucidated.[10,12] Nonetheless, they exhibit appealing properties as anodes, due to high storage capacity and low operating voltage (~0.1 *vs.* Na^+/Na). HCs are generally synthesized from several carbon-rich precursors, both synthetic and natural, through a solid-phase pyrolysis in the temperature range 600–1500 °C.[13,14] Among the precursors, raw biomasses are the most explored feedstocks for HC production, being cheap, renewable, and widely distributed.[15] In particular, lignocellulosic biomasses such as agricultural by-products and forestry residues represent the major waste biomass in the world; only Italy produces around 20 million tons per year of crop by-products and 2 million tons per year of forest residues.[16] In this context, the utilization of lignocellulosic waste for the production of value-added materials such as HCs is beneficial for the sustainability of the SIB industry, and also for agroforestry waste management. However, if on the one hand agricultural by-products are extensively evaluated as a potential precursor for HC production, on the other hand, forest residues are, to the best of our knowledge, less investigated, despite their sharing the same chemical composition as agricultural analogues, being composed of cellulose, hemicellulose and lignin as building blocks of plant cell walls.[17]

Another key component of electrodes is the binder material, which acts as a glue between the active material, conductive agent, and current collector. Although it is generally present in low percentages (2–5% wt),[18] its binding ability and stability ensure prolonged physical and electrical contact within the electrode components, thus improving the cycle life of the cell. An ideal binder should meet some important requirements. Among them, its environmentally friendly nature, low cost, and aqueous processability are becoming crucial properties. Polyvinylidene fluoride (PVDF), the state-of-the-art binder material for LIBs, has some important ecological limitations. Firstly, it is dissolved in the toxic and expensive *N*-methyl-2-pyrrolidone (NMP);[19] secondly, PVDF belongs to the polyfluoroalkyl and perfluoroalkyl substances (PFAS), which are characterized by their highly concerning environmental effects due to their high persistence in ecosystems and bioaccumulation capability in living organisms.[20] In light of these concerns and the recent actions put in place by authorities all over the world to limit the use of PFAS,[21] the research and development of F-free and bio-based binder materials is currently a key topic in the battery industry. In this context, different bio-based binders have been proposed recently, among which the sodium salt of carboxymethylcellulose (Na-CMC) is the most important alternative to PVDF and is gradually replacing it at the anode side.[18] Lignin, the second most abundant biopolymer on Earth, could be another promising binder material for rechargeable batteries, thanks to its chemical structure, being a heterogeneous aromatic polymer with an amorphous 3D network, given its high level of crosslinks and branches.[22] The aromatic skeleton mainly provides structural rigidity and thermal stability; the highly crosslinked structure can ensure robust adhesiveness through mechanical bonding, while the abundant polar functional groups can enable the formation of hydrogen bonds with active material and additives, enforcing the chemical binding ability.[23,24] Beyond the technical aspects, lignin meets other important requirements such as renewability and large abundance worldwide since it is a common by-product of the pulp and paper industry. Globally, the industry produces around 50 million tons per year of lignin, of which 95% is disposed off or used as low-quality fuel, while only 5% is reused for value-added applications.[25] Nonetheless, its application as a binder material has not been explored much so far; to the best of our knowledge, few studies have been done using lignin or its derivatives as a binder in electrode materials for LIBs[25–28] and SIBs.[29] The main issue regarding the use of lignin as a binder is related to its compatibility with active material substrate and common electrolyte solvents, which can result in poor adhesion and instability of the electrode/electrolyte interface. Moreover, the exact molecular structure of lignin, as well as some physical and chemical properties (*i.e.*, molecular weight, solubility, thermal properties), depends on its origin and the extraction method. Therefore, significant efforts are required to assess the feasibility of using lignin as a binder material for rechargeable batteries, especially focusing attention on the electrochemical behavior and stability upon cycling. Among extraction processes, the organosolv method has been considered one of the most promising methods for isolating lignin for producing biomaterials, since it leads to high-quality lignin in terms of purity and sulphur-free nature. For the organosolv extraction, the conventional organic solvents are progressively replaced by novel biomass-derived solvents, such as γ-valerolactone (GVL). GVL is a bio-based, non-toxic, and recyclable solvent that effectively promotes the delignification of biomass when it is coupled in a binary system with water.[30,31] Herein, holm-oak waste (*Quercus Ilex*) has been used as a feedstock for the synthesis of hard carbon and as a lignin source for extraction by a GVL : H_2O mixture. The obtained materials have been combined and used for the production of bio-based anode electrodes that have been tested to assess the feasibility of using organosolv-extracted lignin as a binder material with hard carbon substrates in Na half-cells.

2 Experimental

2.1 Synthesis of holm oak-derived hard carbon

The holm oak waste was collected from the Alte Valli of Rivers Potenza and Chienti, a wooded area in Marche Apennines (Italy). The air-dried sample was sieved to a particle size of <1 mm. The ground biomass was submitted to preliminary water leaching to remove impurities. In detail, the samples were put in deionized water (sample : water ratio 1 : 50) and heated to 60 °C for 12 h under stirring. After that, the biomass was filtered, washed two times with fresh water, and dried at 80 °C overnight. The dried raw material was ground to a fine powder with an

automated ball mill at 300 rpm for 4 h in a steel jar (ball-to-powder ratio 1 : 50 in weight) and carbonized in a horizontal cylindrical furnace at 1000 °C for 2 h under nitrogen flow after a heating ramp of 5 °C min^{-1}. The sample was cooled inside the furnace under nitrogen flow, then submitted to acid leaching in 3 M HCl (sample : solution ratio = 1 : 20) for 3 days under vigorous stirring at room temperature. Finally, the sample was filtered and washed with deionized water until a neutral pH was obtained, then stored at 80 °C overnight. The hard carbon obtained was labelled as LHC.

2.2 Extraction of lignin

The lignin extraction was carried out by broadly performing an organosolv method reported elsewhere.[32] Briefly, the biomass was dried and milled to a particle size <1 mm and suspended in a mixture of GVL with H_2O in the ratio 1 : 1 w/w using a solid-to-solvent ratio of 1 : 10 w:w. The resulting mixture was put into a microwave reactor and heated for 2 h at 170 °C under vigorous stirring. Subsequently, the solution was cooled below 50 °C. After that, the mixture was filtered and the lignin contained in the filtrate ("organosolv liquor") was precipitated using fresh water and collected using centrifugation. The extracted lignin sample was dried in an oven overnight and labelled as LGN.

2.3 Electrode processing and cell assembly

Anodes were made using LHC as the active material, Super-P carbon (Imerys) as the conductive agent, and LGN as the binder. HC : Super-P : Lignin (80 : 10 : 10 w/w) slurries were dispersed in GVL, coated onto Al foil using the doctor blade technique (thickness of wet coating = 100 μm), and left to dry at room temperature. The same procedure has been followed for PVDF- and CMC-based electrodes, except for the dispersion, which was conducted in *N*-methyl-2-pyrrolidone (NMP) and water, respectively. After calendaring, circular electrodes (9 mm diameter) were cut and dried at 120 °C under a vacuum for 12 h. The loadings of active materials were in the range of 0.6–1.0 mg cm^{-2} for all the electrodes. Na half-cells were prepared by assembling three-electrode Swagelok-type cells in an argon-filled glove box (Jacomex GP-campus, oxygen and moisture content less than 0.8 ppm) using LHC-based anodes as the working electrode and metallic sodium (Sigma-Aldrich) as reference and counter electrodes. A 1 M solution of $NaClO_4$ (Sigma-Aldrich) in ethylene carbonate (EC)/propylene carbonate (PC) (1 : 1 in volume) (Sigma-Aldrich) was selected as the electrolyte (400 μl), and 12 mm glass fiber disks (Whatman GF/A) as the separator.

2.4 Material characterizations

The constituent analysis of oven-dried holm-oak feedstock was conducted following the NREL protocols TP-510-42619 "Determination of Extractives in Biomass",[33] and TP-510-42 618 "Determination of Structural Carbohydrates and Lignin in Biomass".[34] Holocellulose content was estimated as the difference between the sum of the other constituents and the total 100% given by the oven-dried sample weight. For the extracted lignin, the TP-510-42618 protocol was used to estimate the purity of the lignin sample and the effectiveness of the extraction. All the determinations were repeated twice. Infrared spectra (FT-IR) of the LGN powder were recorded using a PerkinElmer Spectrum Two FTIR spectrometer within the wavenumber range of 400 to 4000 cm^{-1}. Thermogravimetric analysis (TGA) of LGN was carried out using a PerkinElmer STA 6000 Thermal Analyzer. The nitrogen flow rate at the powder was set to 50 ml min^{-1}, and an alumina crucible was used to hold the sample. After equilibration, the powder was heated to 800 °C at a rate of 10 °C min^{-1}. Gel Permeation Chromatography (GPC) was performed to determine the molecular weight of the lignin binder. An Agilent 1260 Infinity II Multi Detector Suite (MDS) was used for the analysis. The instrument is equipped with a guard column (Agilent GPC/SEC Guard Column) followed by two columns in series (PLgel MIXED-C and PLgel MIXED-D). Three different detectors were installed on the device: a dual light scattering detector (at the angles of 15° and 90°), a refractive index detector, and a viscosity detector. THF was used as the mobile phase, with a flow rate of 1.0 ml min^{-1}. The standards used for column calibration were polystyrene standards with different M_p values in the range of 580–283800 g mol^{-1}. For the measurements and data analysis, Agilent GPC/SEC Software was used. Prior to the analysis, the lignin sample was acetylated using a mixture of glacial acetic acid:acetyl bromide (9 : 1 v/v) for 6 h. The solvent mixture was removed under vacuum, and the acetylated lignin was dissolved in THF (1 mg ml^{-1}). Scanning Electron Microscopy (SEM) and Energy Dispersive X-ray analysis (EDX) of the hard carbon sample and electrodes were acquired using a FESEM Cambridge Stereo scan 360 electron microscope equipped with a QUANTAX EDX detector (at an accelerating voltage of 15 kV). The cycled electrode was washed with dimethyl carbonate before post-mortem analysis. The structure of the hard carbon powder was characterized by X-ray diffraction (XRD) (Bragg–Brentano geometry, Cu-Kα, λ = 1.54059 Å) and Raman spectroscopy (Horiba IHR 320, wavelength 532 nm). The interplanar spacing (d_{002}) was calculated according to Bragg's Law (eqn (1)):

$$d_{002} = \lambda/2 \sin(\theta_{002}) \quad (1)$$

With λ = 0.154 nm. The crystallite size along the *c*-axis (staked plane height) L_c was estimated according to Scherrer's Equation (eqn (2)):

$$L_c = K\lambda/\beta_{002} \cos(\theta_{002}) \quad (2)$$

where K is a shape factor corresponding to 0.9, and β is the full width at half maximum of the (002) peak.[35] Moreover, the average width of the graphene domain L_a was also estimated using the Raman technique according to eqn (3):

$$L_a = (2.4 \times 10^{-10})\lambda^4(I_G/I_D) \quad (3)$$

The pore characteristics of the holm-oak-derived HC were evaluated *via* CO_2 adsorption measurements at 273 K using a Micromeritics ASAP 2020 instrument. Prior to the adsorption, the sample was outgassed for 12 h at 150 °C. The specific surface area was calculated using the BET model, and the Pore

Size Distribution (PSD) was calculated according to the DFT method.

2.5 Electrochemical characterizations

All electrochemical tests were conducted using a VMP-2Z multichannel electrochemical workstation by Bio-Logic Science Instruments (France). Cyclic voltammetry of holm-oak-derived HC electrodes in a Na half-cell was performed at different scanning rates ranging from 0.10 mV s^{-1} to 1.00 mV s^{-1} in the voltage range 0.01 to 2 V *vs.* Na^+/Na. Galvanostatic charge/discharge and rate capability tests of the hard carbon electrodes in Na half-cells were collected with the voltage ranging between 0.01 and 2 V, assuming for all the experiments that 1 C rate corresponds to 300 mA g^{-1} with respect to active material mass. The C-rate capability of the LHC electrodes was evaluated in the C/5 to 5 C range (5 cycles at every rate). In order to evaluate the interfacial behavior of the electrodes, electrochemical impedance spectroscopy (EIS) was carried out at the first cycle and then at each tenth cycle at $E_{we} = 0.4$ V, with an AC amplitude of 5 mV, in a frequency range 100 kHz > f > 10 mHz.

3 Results and discussion

3.1 Chemical, structural, and morphological characterizations of the holm oak-derived hard carbon

The yield % of holm oak pyrolysis to produce hard carbon was calculated to be 22.4% (hard carbon/biomass precursor ratio). However, this value also comprises the residual ashes coming from the biomass precursor. Therefore, EDX analysis was performed on the hard carbon powder obtained by the pyrolysis to estimate the amount of inorganic impurities. The results shown in Fig. 1a reveal, in addition to carbon and oxygen, the presence of heteroelements such as sulphur, chlorine, and especially calcium, accounting for a total atomic percentage of around 1.9 at % in the untreated hard carbon powder. However, since the inorganic impurities strongly affect the structural, textural, and electrochemical properties of hard carbons,[36] acid leaching was performed on holm oak-derived hard carbon powder, and the effectiveness of the leaching to remove the inorganic fraction was evaluated through EDX analysis of the hard carbon obtained after leaching and neutralization. As shown in Fig. 1b and Table 1, the atomic percentage of carbon increased from around 88 at% to 96 at%, as a consequence of the decrease in both the oxygen and calcium contents. This trend suggests that Ca-containing inorganic impurities, such as oxides and/or carbonates, are dissolved in HCl and removed during the filtration. A sensible increase in the Cl atomic percentage was detected due to the residual chlorine after hydrochloric acid leaching. Overall, the sum of the atomic percentage of heteroelements decreased from 1.91% to 0.58 at%. Removal of these inorganic compounds might benefit electrochemical performance because otherwise, they may occupy available active sites for Na uptake, decrease the electronic conductivity, and affect the electrode surface chemistry.[37] For the sake of clarity, the intensities of the Cl and Ca peaks seem to be much higher than that of O in the EPMA spectra (Fig. 1a and b), thus indicating a much higher amount of these heteroelements with respect to O. It should be noted that in the absence of a flat and highly polished surface standard, proper quantification of O cannot be performed; lighter elements (*i.e.*, O and C) generally yield low-energy photons that are susceptible to self-absorption when an energy beam E_0 > 3 keV is employed for the measurement. This phenomenon can lead to a lowering of the intensity of the O peak with respect to other heavier elements, thus underestimating the amount of O when considering relative intensities.[38] In order to deeply evaluate the effectiveness of acid leaching to remove ash, XRD analysis was performed before and after acid leaching, as shown in Fig. 1c and d. The peaks marked with "*", which are present in both non-leached and acid-leached samples, belong to the brass sample holder. On the other hand, the peaks of hard carbon are located at ~22–23° and 43°, which can be assigned to the (002) and (100) crystallographic planes,[39] while the presence of impurities is indicated by the sharp peaks observed for the no-acid treated material, thus evidencing the effectiveness of acid leaching to remove them. Therefore, structural, morphological,

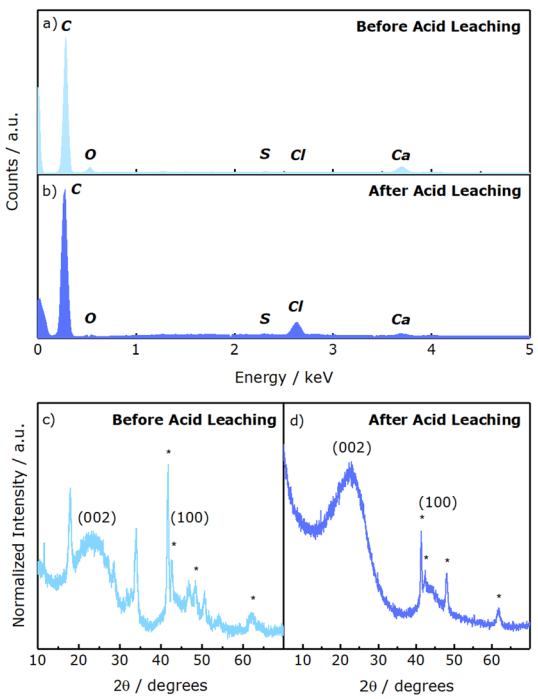

Fig. 1 EDX analysis of holm oak-derived HC (a) before and (b) after acid-leaching. XRD spectra of holm oak-derived HC (c) before and (d) after acid-leaching.

Table 1 Atomic percentage of elements estimated from the EDX analysis of holm oak-derived HC before and after acid-leaching

Sample	Element (at%)				
LHC	C	O	S	Cl	Ca
Before acid leaching	88.50	9.60	0.07	0.07	1.77
After acid leaching	96.84	2.58	0.03	0.46	0.09

and electrochemical characterizations were performed only on acid-leached hard carbon, which will be mentioned only as LHC.

Regarding the above-mentioned characteristic peaks of hard carbon, the (002) band indicates the spacing between graphene layers, and the broadening of the signal is consistent with the presence of short-range structures composed of a random layer lattice with defective sites and crystalline graphitic domains.[40,41] Generally, the synthetic conditions play a primary role in determining the d_{002} of hard carbon with respect to the biomass composition, although the presence of a high ash content in the feedstock is thought to prevent the reorganization of carbon atoms and thus graphitization.[42] The d_{002} of the LHC sample was calculated, according to Bragg's Law reported in eqn (1), as 0.392 nm, in line with other hard carbons reported in the literature.[37,43] This value is higher than that of graphite (0.33 nm) and soft carbon (~0.35 nm), thus facilitating the sodium insertion/de-insertion into hard carbon.

Regarding the other lattice parameters, the stacked plane height L_c is 0.760 nm, while the number of interlayers stacked in the graphitic domains n, estimated according to the calculation $n = L_c/d_{002} + 1$, reveals approximately 3–4 stacked graphene layers in the graphitic domains for LHC.[44] Additional information about LHC powder was obtained using Raman Spectroscopy. As shown in Fig. 2a, the two typical bands of layered carbon are located at around 1336 cm^{-1} (D-band) and 1580 cm^{-1} (G-band). Moreover, two broad and low intensity peaks are located at ~2680 cm^{-1} and 2880 cm^{-1}, corresponding to the second-order bands 2D and D + G, respectively. From the intensity ratio between the G band and the D band (I_G/I_D), the degree of graphitization of LHC was calculated to be 0.96, in line with other hard carbons synthesized at similar annealing temperatures.[45] Although the D band generally reflects the presence of disorder and defects in the sp^2 network of carbon materials, it has been found that for hard carbon with crystallite size L_c below 2.0 nm, such as LHC, the presence of a predominant D band can be correlated with a high level of structural order and limited defect density.[14] From eqn (3), the average width of the graphitic domains L_a was calculated to be 18.46 nm. To further investigate the hard carbon properties, CO_2 adsorption measurements were performed. The obtained isotherm is shown in Fig. 2b, while the calculated DFT pore size distribution is shown in Fig. 2c. The value of the CO_2 BET specific surface area (SSA) was calculated to be 320.3 $m^2\ g^{-1}$; this relatively large SSA is expected to promote considerable electrolyte decomposition during the first sodiation, decreasing the initial coulombic efficiency % (ICE) of the hard carbon. However, since CO_2 can also detect the narrowest micropores, their presence in the sample "apparently" increases the calculated SSA with respect to the common SSA values obtained with N_2, which cannot access them. The DFT pore size distribution confirms the presence of a certain moiety of micropores, with most of the micropores having sizes described by a Gaussian-type curve in the 0.4–0.7 nm range, representing around 78%

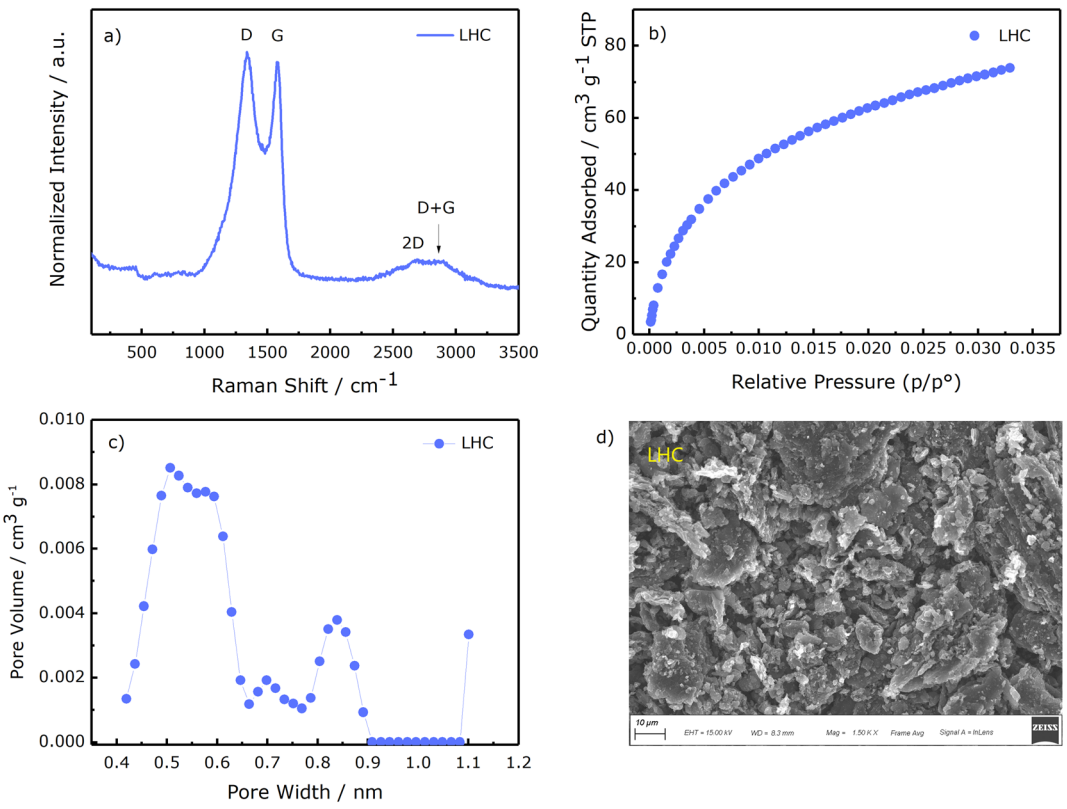

Fig. 2 Chemical and morphological characterizations of LHC powder: (a) Raman spectra; (b) CO_2 adsorption–desorption isotherm; (c) pore size distribution and (d) SEM image. Magnification: 1500×.

Table 2 Structural and physical properties of LHC

d_{002} (nm)	L_c (nm)	L_a (nm)	I_G/I_D	n	SSA CO_2 (m^2 g^{-1})
0.392	0.760	18.46	0.960	3.49	320.3

of the total volume created by micropores with sizes ≤1.1 nm. These so-called "ultramicropores" are involved in Na^+ storage, providing extra sites for sodium adsorption.[46] The SEM image (Fig. 2d) of LHC powder reveals an irregular particle size distribution in the micrometer range with a flake-like morphology. All the structural parameters of the acid-leached LHC powder are summarized in Table 2.

3.2 Extraction, chemical, and structural characterizations of the holm oak-derived lignin binder

Before extraction, compositional analysis of the holm oak feedstock was performed to assess the lignin content (Table 3). Since the holm oak waste used in this work is composed of wood and bark, the contents of the extractives in the form of waxes, resins, gums, soluble sugars, starches, *etc.*, were expected to be relevant and higher than those of bark-free samples. The total amount of lignin, expressed as the sum of Klason lignin and acid-soluble lignin, was 29.2%, comparable with other woody precursors in the literature.[37] The acid-soluble lignin, which is generally composed of the low-molecular-weight fraction of lignin,[47] represents a small fraction of the holm oak total lignin content, and is expected to deteriorate the performance of lignin when used as the binder material for SIBs, since low-molecular-weight fractions can be solubilized in electrolyte solvents.

Table 3 Macromolecular composition of holm oak feedstock

Extractives %	Klason lignin %	Acid-soluble lignin %	Holocellulose %	Ash %
11.4	21.6	7.6	58.1	1.3

The extraction of lignin binder was performed using the organosolv separation method described in Section 2.2. This method involves the breaking of lignin-carbohydrate complex (LCC) linkages, followed by the hydrolysis of glycosidic bonds of hemicellulose and depolymerization of lignin through the cleavage of ether bonds, promoting the dissolution of lignin.[48] An insoluble cellulose-rich fraction in the solid residue and an organosolv liquor containing both lignin and water-soluble compounds, such as sugars (mainly hemicellulose monomers) and carbohydrate decomposition products, were obtained.[49]

The lignin in the filtrate was separated with the addition of fresh water, which promoted its precipitation.[32] The process is schematized in Fig. 3. The isolated lignin yield, calculated with respect to the weight of the starting biomass, was 13.9%; this means that around 48% of the total lignin content in holm oak and 64% of the acid-insoluble lignin can be recovered by precipitation. The effectiveness of lignin dissolution can be explained by the Hildebrand and especially the Hansen solubility parameters (δ). The Hildebrand δ of lignin ranges between 21.0 and 25.0 $MPa^{1/2}$,[50] while that of GVL is 23.1 $MPa^{1/2}$.[31] Therefore, according to the Hildebrand parameters, GVL has a high affinity for lignin. However, for polar molecules such as GVL, Hansen Solubility Parameters (HSP) are more realistic since they take the contributions of the hydrogen bond ability and polar nature of the molecules into account.[49] According to the Hansen theory, a practical way to evaluate how close the solubility parameters of two substances are to each other is by calculating the Hansen Relative Energy Difference (RED), which is a parameter describing the compatibility between solvent and solute, the details and calculations of which are reported elsewhere.[51] Briefly, a good solvent has a RED value lower than 1, while a bad solvent has a RED value higher than 1. In this case, the Hansen relative energy difference between lignin and GVL is 0.83,[52] thus indicating that the solvent can solubilize lignin. Moreover, the RED value of GVL and lignin reached 0.58 when

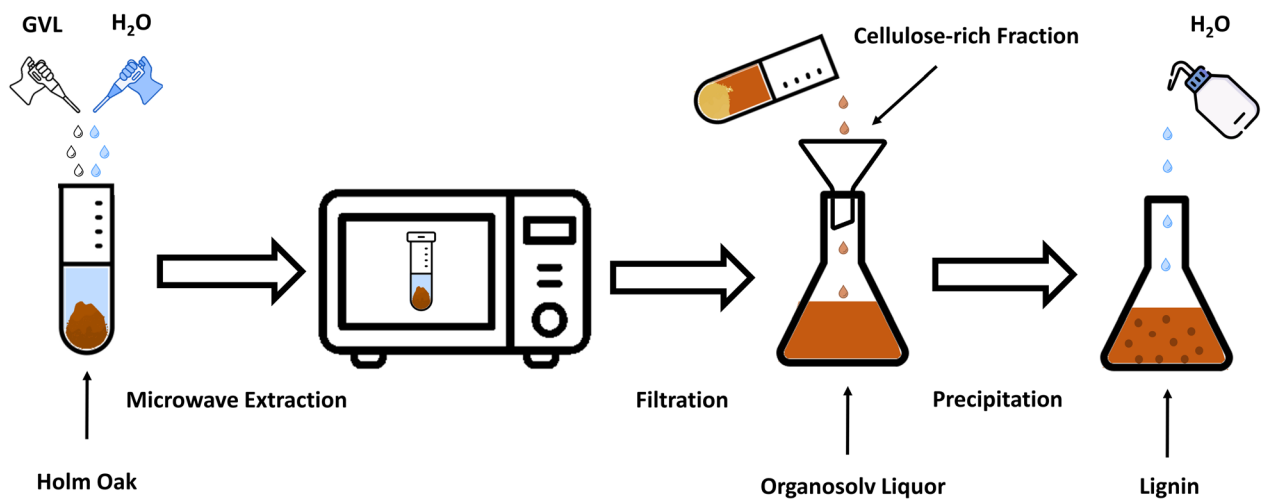

Fig. 3 Schematic of lignin extraction.

a mixture of 80% GVL and 20% H_2O was used.[30] These results are the consequence of the enhanced hydrogen bonding capability of the solvent system, which allows easier and stronger hydrogen bonding interactions between the solvent system and lignin, replacing the intermolecular hydrogen bonds in lignin and, therefore, promoting the dissolution.[53] According to the Hansen RED, the optimal solubility should be achieved at GVL 80% and H_2O 20%; however, experimental results showed that the maximum extent of lignin dissolution was obtained using a water content in the range of 35–50%.[31,32] These results can be related to the higher H-bonding ability, which is maximum at a GVL concentration of 50–60%, providing more hydrogen bonds with respect to pure GVL; however, excessive water makes the interaction between γ-valerolactone and water molecules stronger, thus hindering the formation of hydrogen bonds with lignin.[54,55]

Table 4 Chemical composition of lignin recovered from the organosolv liquor

Klason lignin %	Acid-soluble lignin %	Total lignin %	Ash %	Others %
85.5	9.7	95.2%	0.7	4.1

To estimate the purity of the isolated lignin, Klason lignin, acid-soluble lignin, and ash content percentages were measured according to the TP-510-42618 protocol. As shown in Table 4, the purity of recovered lignin was estimated as 95.2% (85.5% if only Klason lignin is considered). The purity of the obtained lignin is in the range of other organosolv lignins isolated using different raw materials and solvents.[56–58] Ash and residual carbohydrates impurities are below 5%.

FT-IR spectra of extracted lignin are shown in Fig. 4a, and the respective peak assignments are summarized in Table S1. The broad band in the range 3550–3100 cm^{-1} is attributed to the O–H stretching of phenolic and alcoholic groups.[26] The 2938 cm^{-1} and 2837 cm^{-1} peaks are attributed to C–H stretching in $-CH_2^-$ and $-CH_3$, respectively. The band with two ticks at around 1730 cm^{-1} can be assigned to the C=O stretching of the residual acetyl group of hemicellulose[52] and the unconjugated carbonyl group.[57] The region of aromatic backbone vibrations (~1600–1250 cm^{-1}) contains different

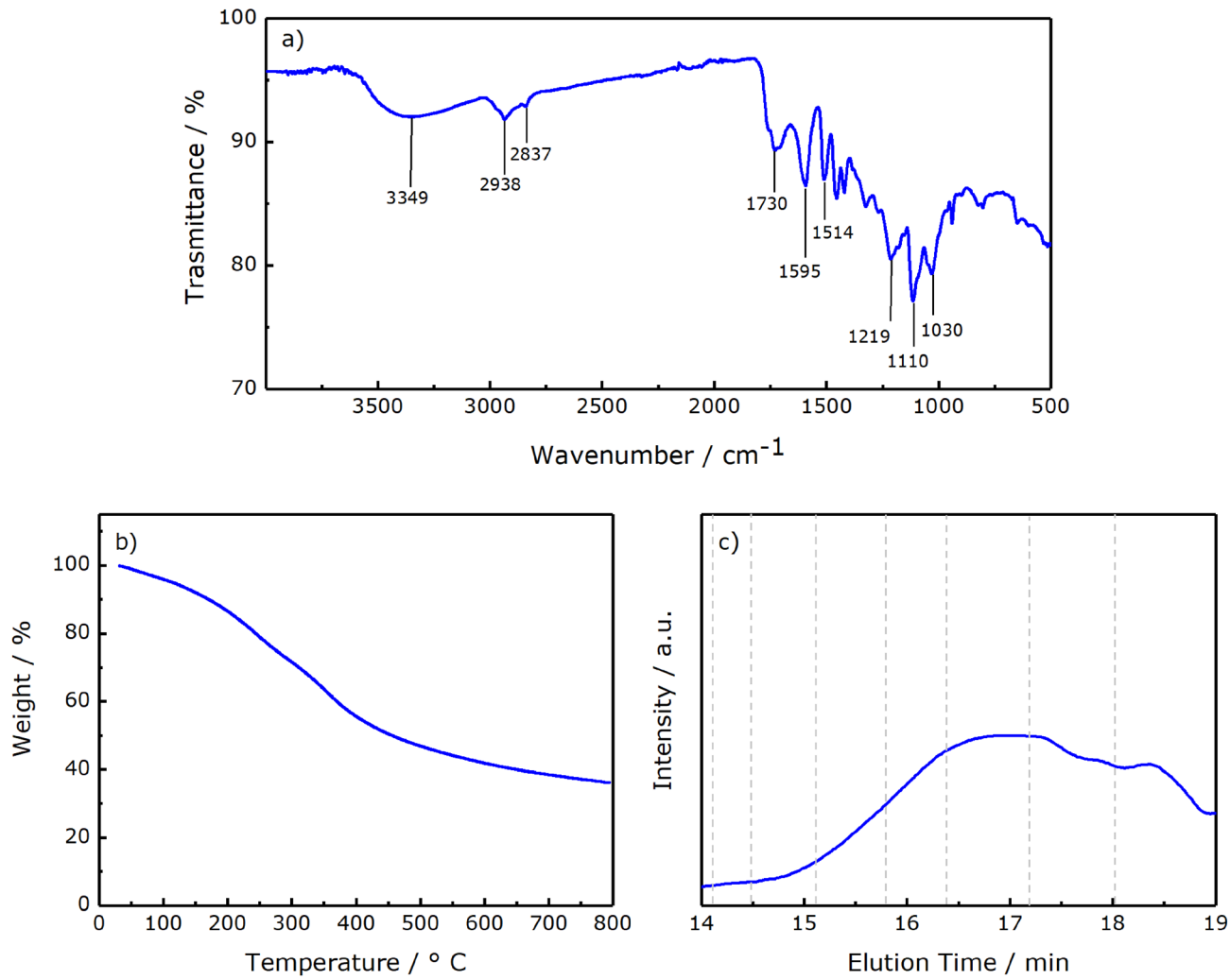

Fig. 4 Characterizations of holm oak-extracted lignin: (a) FT-IR spectra; (b) TGA analysis; and (c) GPC chromatogram.

peaks with different intensities. Syringyl units (*S*) of lignin show typical bands at 1595 cm^{-1}, 1326–1324 cm^{-1}, and 1110 cm^{-1}, which are assigned to the aromatic skeletal vibrations, S ring breathing, and aromatic C–H in-plane deformation of *S* units, respectively. On the other hand, guaiacyl units (*G*) of lignin exhibit the above-mentioned vibrations with bands at 1524 cm^{-1}, 1257 cm^{-1}, and 1030 cm^{-1}, respectively.[58] The band at 1219 cm^{-1} is attributed to the C–O stretching of the characteristic aryl and alkyl ether linkages of lignin. The thermal behavior of the isolated lignin was characterized using thermogravimetric analysis (Fig. 4b). Generally, lignin has a high thermal stability and decomposes slowly in a wide temperature range from room temperature to 800 °C, leaving a considerable amount of solid residue.[59] Nonetheless, different stages of degradation can be distinguished. At the first stage (around 100 °C), the weight loss can be attributed to the moisture retained in the samples. The next stage, which occurs in the temperature range 180–300 °C and leads to a weight loss of around 17.4%, can be attributed to the degradation of residual impurities of carbohydrates in the lignin sample, which are converted to volatile gases such as CO, CO_2, and CH_4, or the start of lignin decomposition. The latter becomes the main phenomenon in the temperature range 300–450 °C, where the fragmentation of inter-unit linkages releases monomers and low-molecular-weight derivatives of phenol into the vapor phase,[60] producing a weight loss of 21.1%. As the temperature is further increased (over 450 °C), the decomposition and condensation of aromatic rings occur, leading to the formation of char, which gives solid residues of around 36%.[52,60] The molecular weight distribution of the derivatized lignin sample was measured with GPC. The calculated number-average molecular weight (M_n), weight-average molecular weight (M_w), and polydispersity index (PDI) are reported in Table S2. The vertical and dotted lines in Fig. 4c represent the elution times for some of the polystyrene molecular weight standards used for calibration. The broad curve in the GPC chromatogram and the PDI value of 2.6 reflect the heterogeneity among lignin chain lengths, as a result of the simultaneous occurrence of lignin depolymerization and recondensation reactions during GVL organosolv extraction.[30] The weight-average molecular weight M_w was estimated to be 2156 g mol^{-1}, which is well below the typical range of milled wood lignin (5500–20 000 g mol^{-1}).[24] This suggests that the reaction severity, *i.e.*, reaction temperature and time, largely promotes depolymerization reactions. Overall, the obtained M_w and M_n are comparable with other lignins extracted by GVL from different biomasses (Table S2).

3.3 Electrochemical characterizations

Cyclic voltammetry (CV) during the initial three cycles was performed on holm oak-derived hard carbon coupled with lignin binder to assess the topotactic reaction of Na^+ in LHC. The analysis was performed at a scanning rate of 0.10 mV s^{-1} in the potential range $0.01 < E_{we} < 2.00$ V using metallic sodium as reference and counter electrodes. As shown in Fig. 5a, during the first cathodic scan, an irreversible broad peak (*A*) extends from approximately 1.00 V to 0.20 V, assigned mainly to the decomposition of the electrolyte and the formation of the SEI, which is mainly responsible for low ICE.[61] In the following scans, the contribution from irreversible SEI formation disappears, leaving a reversible broad peak (*B*) at potential values between 0.90 and 0.10 V and a narrow and reversible peak (*C*) centered at around $E_{we} = 0.01$ V. Although there is still an ongoing debate regarding the sodium storage mechanism in hard carbon, the broader-potential-range feature marked as *B* may be largely associated with the adsorption of sodium ions at surface active sites,[62] while the low-voltage peak may be attributed mainly to the Na^+ intercalation into hard carbon graphene layers. Also, the contribution of pseudocapacitive processes related to the internal pore filling by Na must be taken into account, especially at potentials approaching the cut-off of 0.01 V.[63] During the anodic scans, the oxidation peaks (*C′*) and the broad feature (*B′*) indicate the reversibility of the electrochemical processes. After the 1st cycle, the CV curves overlapped, confirming the reversibility of processes described by the *B*/*B′* and *C*/*C′* features. To further investigate the Na storage mechanism of hard carbon, cyclic voltammograms were recorded and different scan rates between 0.1 mV s^{-1} and 1.0 mV s^{-1} (Fig. S1a), and the power–law relationship was used to discriminate between surface-controlled and diffusion-controlled reactions by fitting the experimental data to the following equation (eqn (4)):[64]

$$i = av^b \tag{4}$$

where *i* is the peak current, *v* is the scanning rate, and *a* and *b* are constants to be determined. The *b* value can be obtained by calculating the slope of the linear fit of $\log i$ *vs.* $\log v$ according to eqn (5):

$$\log i = b \log v + \log a \tag{5}$$

Typically, a value of *b* close to 0.5 indicates a diffusion-controlled reaction, while a value of *b* close to 1 indicates that the current is controlled by capacitive behavior. Here, two peaks were considered: the first one is the broad peak at 0.5 V (i_s) corresponding to the sloping region, while the second one is the sharp peak in the low potential region at 0.01 V (i_p). Fig. S1b shows an excellent linear relationship ($R^2 = 0.99$) for both curves between current peaks and scan rate on the logarithmic scale. The obtained *b*-values were 0.84 for i_s and 0.54 for i_p, respectively. Thus, these results suggest that the current in the sloping region (i_s) mostly arises from the surface-controlled reactions, such as adsorption on surface active sites, while the current at low potentials (i_p) originates from the diffusion-controlled reaction (*i.e.*, sodium insertion/extraction between graphene layers). Additionally, the capacitive contribution to the current response can be determined according to the following equation (eqn (6)):

$$i(V) = k_1 v + k_2 v^{1/2} \tag{6}$$

where the current response at a fixed potential can be differentiated into capacitive-controlled ($k_1 v$) and diffusion-

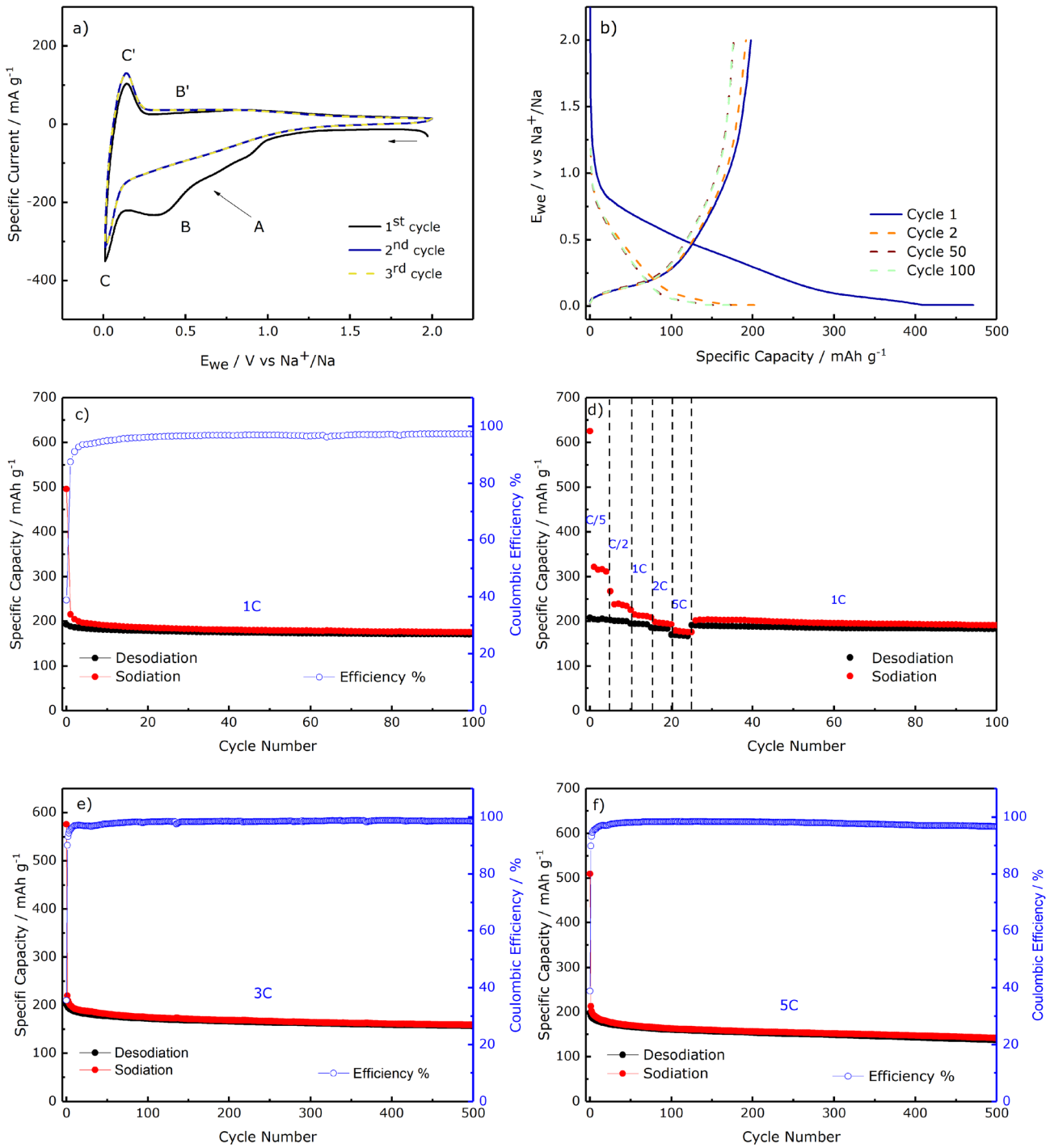

Fig. 5 Electrochemical characterization of LHC-LGN composite electrode in Na half-cells: (a) cyclic voltammetry curves upon the first three cycles at a scan rate of 0.1 mV s^{-1}; (b) galvanostatic profiles of charge/discharge of the cell cycled at 1 C; (c) cycling at 1 C; (d) rate capability; and long cycling at (e) 3 C and (f) 5 C.

controlled ($k_2\nu^{1/2}$) contributions. The contribution of the two mechanisms to the current response can be determined from k_1 and k_2.[65] Fig. S1c shows the trends of capacitive and diffusive contributions (%) as a function of potential (V) at a scan rate of 0.1 mV s^{-1}. As expected, during sodiation, the capacitive contribution % is maximum at 0.75 V (81.5%) and then progressively decreases, reaching a minimum at 0.05 V (19.4%). These results suggest that at low-potential ($E_{we} \leq 0.15$ V), the main process is the diffusion-controlled intercalation of Na^+ into hard carbon with a non-negligible contribution of the pseudocapacitive process, while in the sloping region ($0.35 \leq E_{we} \leq 0.75$ V), pseudocapacitive processes govern the charge storage. The galvanostatic charge and discharge profiles E *vs.* Q of the LHC-LGN composite electrode, cycled at a current density of 300 mA g^{-1} in the potential range $0.01 < E_{we} < 2.00$ V, shown in Fig. 5b, confirm the typical pattern of hard carbon Na storage

evidenced by CV. A pseudo-plateau starting at around 0.80 V (corresponding to broad peak A in CV), due to the electrolyte decomposition and solid electrolyte interphase (SEI) formation, was observed.[10] The associated irreversible capacity loss is remarkable (around 273 mA h g^{-1}), corresponding to an ICE of 42%. As in CV, this feature disappears in the subsequent cycle, indicating that a relatively stable SEI was formed[40] and no additional parasitic reactions occurred. On the other hand, the sloping potential profiles were approximately between 0.80 and 0.10 V during reduction and between 0.30 and 1.00 V during oxidation (corresponding to B/B' broad features in CV) and the low-potential plateau (corresponding to C/C' narrow peaks in CV), are highly reversible upon cycling. This confirms the reversibility of the sodium uptake/removal, as well as the maintenance of electrode integrity, as demonstrated by the capacity retention of 91.1% at 100 cycles. Fig. 5c details the charge/discharge behavior over 100 cycles. The electrode delivers a discharge capacity of 496.0 mA h g^{-1} that decreases in the second discharge to 215.5 mA h g^{-1}. The irreversible electrolyte decomposition and Na^+ ion trapping into the HC matrix led to a poor ICE % of 38.9%.[66] One explanation of this poor ICE can be found in the high specific surface area of the holm oak-derived HC, which inevitably offers a large exposed surface to the electrolyte decomposition, and also in the high concentration of surface defects, particularly oxygen-containing functional groups as revealed by the EDX analysis of LHC, which can promote the decomposition of the electrolyte.[67,68] Nonetheless, the LHC-LGN composite electrode exhibited a progressive increase in the reversibility of the sodiation/desodiation process after 10 cycles, since the specific capacity tends to stabilize at about 180 mA h g^{-1}. The cell retained 90.6% of its capacity after 100 cycles. In order to evaluate the impact of the lignin binder on the electrochemical performances of the hard carbon electrode, a comparison of the cycling performances of the LHC-LGN composite electrode with two well-established binders (PVDF and CMC) was carried out. As shown in Fig. S2 and detailed in Table S3, all three electrodes displayed poor ICE % values, where the lignin-based electrode exhibited the lowest ICE % (38.9%), followed by PVDF (42.6%) and CMC (45.3%). These results suggest that the binder has a relative impact on the decomposition of the electrolyte since no significant variations were encountered between these different binders. Therefore, the high SSA of LHC active material is mainly responsible for the low ICE %. However, for the sake of clarity, the average coulombic efficiencies of all cells are not yet adequate for practical application since none reached values above 99.5%, where that of the LGN-based electrode is in the range 97–98%. This could be ascribed either to limitations coming from the half-cell setup (*i.e.*, the presence of Na metal rather than a cathode) and to the lab-scale manufacture of the electrode, which can underestimate the electrochemical performances of the cell and, in particular, its stability. However, these aspects can be carefully optimized during scale-up and full cell optimization.[69] Not even the CMC- and PVDF-based electrodes reached satisfactory coulombic efficiencies, with the latter also encountering capacity fluctuations after around 55 cycles, probably ascribed to the instability of the electrode/electrolyte interface. Nonetheless, the specific capacity and capacity retention of the lignin-based electrode are comparable with those obtained with PVDF- and CMC-based electrodes, which are of significant importance for further developments. To deeply assess the electrochemical performances of holm oak-derived hard carbon with γ-valerolactone-extracted lignin binder, a rate capability test was performed at selected cycling rates in the range C/10 to 5 C, as shown in Fig. 5d. The poor coulombic efficiency of the initial low-current rate cycles is the result of the favored electrolyte decomposition under slow kinetics.[70] Nonetheless, the LHC-LGN exhibits a promising rate capability, experiencing low-capacity fade when the current is increased. The average discharge capacities are 315.9, 243.1, 215.5, 198.9, and 180.7 mA h g^{-1} at C/5, C/2, 1 C, 2 C, and 5 C, respectively. Restoring the current to 1 C for up to 100 overall cycles yields a specific capacity above 190 mA h g^{-1} after 100 cycles, with a reversibility of the charge/discharge processes at 1 C (300 mA g^{-1}) in line with that already evidenced in Fig. 5c. To further evaluate the ability of lignin binder to guarantee long cycle life, even in demanding conditions, galvanostatic cycles were performed on LHC-LGN composite electrodes at current densities of 900 mA g^{-1} (3 C) and 1500 mA g^{-1} (5 C). As shown in Fig. 5e and f, under both conditions, the LHC-LGN cells are characterized, during the initial cycles, by a low coulombic efficiency due to SEI formation at the hard carbon surface. Nonetheless, after cell activation, both cells deliver high specific reversible capacities (220.0 and 213.3 mA h g^{-1} at 3 C and 5 C, respectively), as well as long cycling stability, as demonstrated by capacity retention values of 86.8% and 83.7% after 100 cycles and 79.1% and 71.6% after 500 cycles for cells cycled at 3 C and 5 C, respectively. It should be noted that in any cycling conditions at 1 C, 3 C, and 5 C, no spikes in the desodiation capacity, ascribable to possible SEI dissolution/reformation, were observed, suggesting the long-term stability of the passivation layer. Relevant results are summarized in Table 5. Overall, all these results suggest the ability of the lignin binder to guarantee electrode integrity

Table 5 First cycle discharge capacities, initial coulombic efficiencies %, second cycle discharge capacities, and capacity retentions after 100 cycles of LHC-LGN composite electrodes at different current rates

Electrode	Discharge capacity 1st cycle (mA h g^{-1})	ICE (%)	Discharge capacity 2nd cycle (mA h g^{-1})	Capacity retention after 100 cycles (%)
1 C	496.0	38.9	215.5	90.6
3 C	575.8	35.6	220.0	86.8
5 C	509.5	38.8	213.3	83.7

during cycling, ensuring high-capacity retention and long cycle life. Taking into account the relatively low molecular weight measured for the extracted lignin, the good binding ability of lignin binder is not expected to be given only by the mechanical interlocking mechanism such as in PVDF, but more plausibly and at larger extent by the intermolecular forces, especially the H-bonds between the polar functional groups of lignin and the oxygen-containing functional groups of hard carbon.[71]

Additional information about the electrode integrity after 100 cycles was obtained by performing SEM morphological investigations on the pristine and cycled electrode (Fig. 6a and b). Inevitably, the morphology of the pristine electrode showed different textures with respect to the cycled electrode, also in light of the different spots analyzed. However, the rough and inhomogeneous surface of the pristine electrode was maintained after cycling, since no significant morphological changes were detected in the cycled electrode. Notably, the cycled electrode had no visible cracks, confirming its integrity and the ability of the lignin binder to guarantee longstanding adhesion.

To better investigate the electrode kinetics and electrode/electrolyte interfacial behavior of the LHC-LGN composite electrode, potentiostatic impedance spectroscopy measurements were performed at the second cycle and every 10th cycle at $E_{we} = 0.4$ V upon sodiation. The bias potential to be applied during impedance measurements was evaluated by inspecting $dQ\ dE^{-1}$ differential curves (obtained by differentiating the electrode galvanostatic profiles at different cycles). As shown in Fig. 7a, a potential $E_{we} = 0.40$ V was chosen, where the voltage oscillations applied during the impedance measurements were expected to produce limited current oscillations. Consequently, the system is expected to respect the pseudolinearity, causality, and stationarity boundary conditions required for meaningful impedance measurements. The obtained Nyquist plots are shown in Fig. 7b. All the impedance spectra are characterized by an intercept with the real axis in the high-frequency region, a first semicircle in the high-to-medium-frequency region, a second semicircle in the middle-to-low-frequency region, and a straight line in the low-frequency region. The EIS data were modeled through an equivalent circuit model, $R_{el}(R_{SEI}C_{SEI})(R_{ct}$-$C_{dl})WC_i$, using Boukamp's notation.

In detail, the intercept with the real axis describes the Na^+ migration through the electrolyte and has been modeled as a pure resistive element R_{el}; the first semi-circle represents the Na^+ migration through the SEI layer, involving charge accumulation around its surface, hence it was modeled with a resistive element (R_{SEI}) in parallel with a capacitive element (C_{SEI}); the second semi-circle can be ascribed to the faradaic charge transfer process, which is accompanied by the electric double layer at the active material/electrolyte interface, and was modeled with a resistive element (R_{ct}) in parallel with a capacitor (C_{dl}); finally, the low frequency line describes a semi-infinite diffusion to a blocking electrode and it was modeled as a Warburg impedance element (W) in series with a capacitor (C_i), indicating the intercalation capacitance. The values of the parameters related to the model circuit elements were calculated by performing a nonlinear least squares (NLLS) fitting

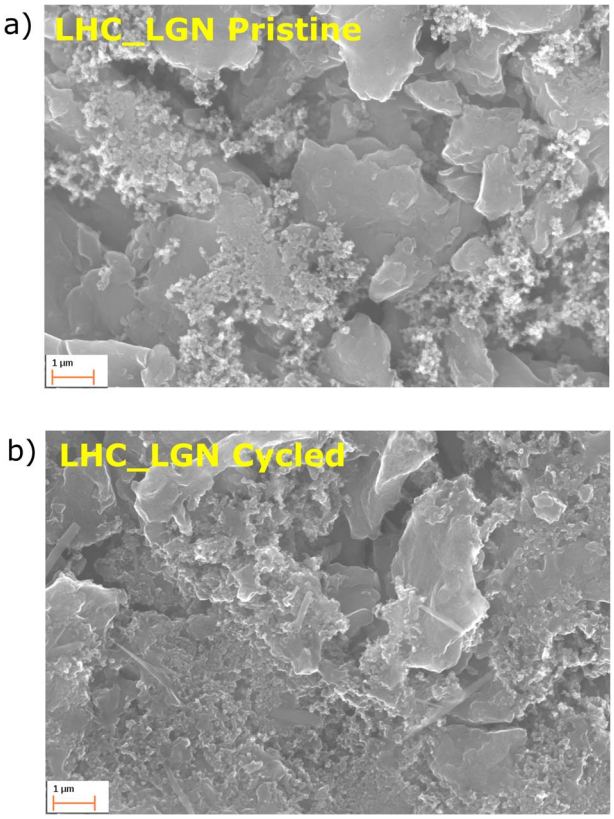

Fig. 6 SEM images of the (a) pristine and (b) cycled electrodes. Magnification 200 00×.

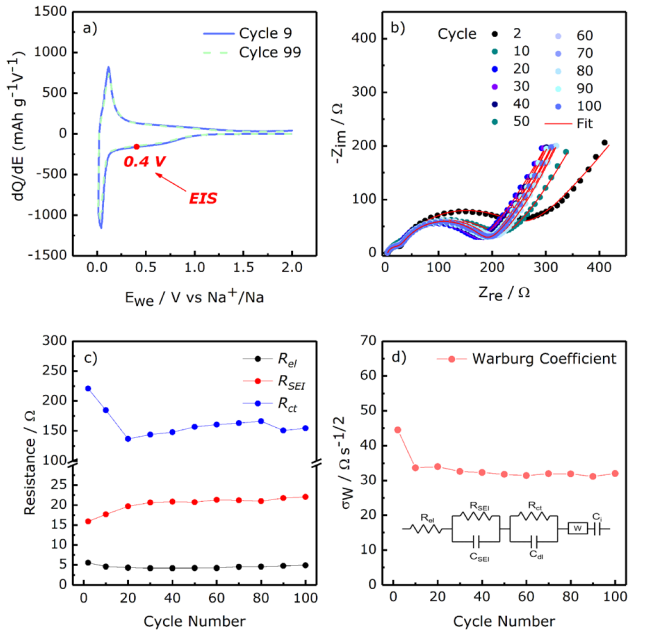

Fig. 7 (a) $dQ\ dE^{-1}$ *vs.* E_{we} curves at different cycles. (b) Nyquist plots of LHC-LGN electrode acquired at the second cycle and every 10th cycle, $E_{we} = 0.4$ V, 100 kHz > f > 10 mHz. (c) Values of R_{el}, R_{SEI}, and R_{ct} upon cycling, as obtained from EIS data analysis. (d) Warburg coefficient values as a function of cycle number. Inset: equivalent circuit used to simulate the data.

Table 6 Numerical values of R_{el}, R_{SEI}, R_{ct}, and the corresponding χ^2 obtained during NLLS analysis

Cycle number	R_{el} (Ω)	R_{SEI} (Ω)	R_{ct} (Ω)	χ^2
2	5.49	15.91	220.58	3×10^{-4}
10	4.56	17.65	184.46	3×10^{-5}
20	4.31	19.70	136.41	7×10^{-5}
30	4.20	20.63	143.65	5×10^{-5}
40	4.18	20.86	147.80	5×10^{-5}
50	4.21	20.73	156.64	4×10^{-5}
60	4.20	21.31	160.30	3×10^{-5}
70	4.51	21.20	163.05	4×10^{-5}
80	4.57	20.99	166.11	5×10^{-5}
90	4.72	21.77	150.48	6×10^{-5}
100	4.85	22.07	154.29	6×10^{-5}

with the Relaxis3 software, where the pure capacitive elements were replaced by constant-phase elements Q to take into account electrode surface roughness and inhomogeneity.[72] The trends of the calculated R_{el}, R_{SEI}, and R_{ct} upon cycling are shown in 7c, while the respective numerical values of resistances are detailed in Table 6. Only NLLS fits of the Nyquist plot with χ^2 in the order of 10^{-4} or below were considered.[73] Beyond the electrolyte resistance (R_{el}), which was stable throughout the cycling, LHC-LGN electrode showed an initial increase of SEI resistance, indicating the progressive formation of the passivation layer at the electrode/electrolyte interface. After 10 cycles, R_{SEI} was stabilized, suggesting the completion of the formation of a stable SEI, preventing further electrolyte decomposition. This trend is consistent with the results obtained during galvanostatic cycling (Fig. 5c and e), where the irreversible contributions to capacity progressively decreased during the first cycles while the coulombic efficiencies increased as a consequence of SEI formation.

The charge-transfer resistance, R_{ct}, sharply decreased during the first 20 cycles, probably as a consequence of the electrode activation due to progressive pore surface wetting by the electrolyte. The R_{ct} was stabilized at around 150 Ω, revealing the stabilization of the reaction kinetics at the electrode/electrolyte interface. The impedance results explain both the good rate capability and cycling stability obtained for LHC-LGN electrodes cycled at different current rates. Finally, the Warburg coefficient σ_W (Fig. 7d) decreased from cycle 2 to cycle 10 and then remained almost constant upon cycling, indicating a stable solid-state diffusion of Na^+ ions into the bulk of the electrode. This trend suggests that after interface activation and SEI formation, no particle agglomeration or other significant textural changes occurred in LHC-LGN electrode during cycling.

4 Conclusions

Herein, we have demonstrated the feasibility of using holm-oak as a feedstock for preparing electrode materials for sodium-ion batteries. Hard carbon was synthesized by one-step pyrolysis followed by acid leaching to remove the inorganic impurities. The chemical, structural, and morphological characterizations revealed that the obtained hard carbon possesses a low atomic percentage of heteroelements (mostly oxygen) and a large interlayer distance (0.392 nm), which is favorable for sodium insertion/extraction; moreover, it has a high SSA and well-developed microporosity, which are beneficial for sodium pseudocapacitive storage but detrimental for the initial coulombic efficiency of the electrode. In parallel, a lignin sample was extracted by the organosolv method using a γ-valerolactone:water mixture, and then used as a binder material. The performed extraction precipitated no more than 64% of the total lignin in the raw material. Nonetheless, the obtained lignin is characterized by a high level of purity and relatively low molecular weight, suggesting that the binding ability is mainly provided *via* chemical bonding, such as the H-bonds between the polar functional groups of lignin and the oxygenated surface functional groups of hard carbon, establishing strong interactions. When the two materials were combined in an anode for SIBs, they exhibited good electrochemical performances, delivering specific capacities of around 200 mA h g^{-1} and long cycling stabilities at different current rates. These behaviors were corroborated by SEM images before and after cycling, and by impedance spectroscopy analysis during cycling. The former confirmed the electrode integrity, with no visible particle agglomeration and morphological changes, and the latter mainly evidenced the electrode/electrolyte interface stability and almost constant reaction kinetics during cycling. Overall, these results show that hard carbon, with excellent Na storage performance, and the lignin binder, with longstanding adhesion, can be developed from natural sources such as holm oak waste in environmentally friendly and cost-efficient ways. Nonetheless, future studies can assess the suitability of using lignin binder at the cathode side, where the replacement of PVDF and NMP processing currently represents an open challenge. The water sensitivity of typical cathode materials, *i.e.*, layered oxides, does not allow the use of the water-soluble sodium carboxymethylcellulose (CMC), which also suffers from a small electrochemical stability window, inherently hindering the use of high-voltage layered oxide cathodes in SIBs.

Author contributions

All the authors contributed to this work and approved the final version of the manuscript. L. B., F. N., A. C and S. G. conceptualized the work. L. B and F. N. wrote the manuscript draft. L. B., H. D., F. V. and G. P. performed the laboratory activities. L. B., H. D., L. S., A. S., L. M. contributed to the analysis and discussion.

Conflicts of interest

There are no conflicts to declare.

Data availability

The produced data supporting the findings of this study are available within the article and its SI. Raw data that support the

findings of this study are available from the corresponding author, upon reasonable request.

Supplementary information containing part of the data supporting this article is available. See DOI: https://doi.org/10.1039/d5se00645g.

Acknowledgements

Authors acknowledge the financial support from projects "ORgANics for Green Electrochemical Energy Storage Project (ORANGEES)", funded by MASE "PT 2019-2021, DD 27.10.2021 Bando A, DD 05.08.2022" and "Green Electrolyte and Biomass-derived Electrodes for Sustainable Electrochemical Storage Devices (GENESIS)", funded by Ministero dell'Università e della Ricerca, within the PRIN 2022 program (DD 104 02.02.2022).

References

1 J. Janek and W. G. Zeier, *Nat. Energy*, 2016, **1**, 1–4.
2 K. W. Beard and T. B. Reddy, *Linden's Handbook of Batteries*, McGraw-Hill, New York, 2019.
3 J. Deng, C. Bae, A. Denlinger and T. Miller, *Joule*, 2020, **4**, 511–515.
4 B. E. Lebrouhi, S. Baghi, B. Lamrani, E. Schall and T. Kousksou, *J. Energy Storage*, 2022, **55**, 105471.
5 H. Pan, Y. S. Hu and L. Chen, *Energy Environ. Sci.*, 2013, **6**, 2338–2360.
6 V. Palomares, P. Serras, I. Villaluenga, K. B. Hueso, J. Carretero-González and T. Rojo, *Energy Environ. Sci.*, 2012, **5**, 5884–5901.
7 T. Liu, Y. Zhang, Z. Jiang, X. Zeng, J. Ji, Z. Li, X. Gao, M. Sun, Z. Lin, M. Ling, J. Zheng and C. Liang, *Energy Environ. Sci.*, 2019, **12**, 1512–1533.
8 *Trading Economics*, https://tradingeconomics.com/.
9 I. Hasa, J. Barker, G. Elia and S. Passerini, *Sodium-ion Batteries: History, Development, and Overview on Market and Application*, Elsevier B.V., 2nd edn, 2023.
10 L. Bottoni, H. Darjazi, L. Sbrascini, A. Staffolani, S. Gabrielli, G. Pastore, A. Tombesi and F. Nobili, *ChemElectroChem*, 2023, **10**, 1–11.
11 J. Y. Hwang, S. T. Myung and Y. K. Sun, *Chem. Soc. Rev.*, 2017, **46**, 3529–3614.
12 X. Chen, C. Liu, Y. Fang, X. Ai, F. Zhong, H. Yang and Y. Cao, *Carbon Energy*, 2022, 1–18.
13 J. Górka, C. Vix-Guterl and C. Matei Ghimbeu, *C*, 2016, **2**, 24.
14 U. Mittal, L. Djuandhi, N. Sharma and H. L. Andersen, *J. Phys.: Energy*, 2022, **4**(4), 042001.
15 K. L. Hong, L. Qie, R. Zeng, Z. Q. Yi, W. Zhang, D. Wang, W. Yin, C. Wu, Q. J. Fan, W. X. Zhang and Y. H. Huang, *J. Mater. Chem. A*, 2014, **2**, 12733–12738.
16 J. Gupta, M. Kumari, A. Mishra, W. Swati, M. Akram and I. S. Thakur, *Chemosphere*, 2022, **287**, 132321.
17 F. Wang, D. Ouyang, Z. Zhou, S. J. Page, D. Liu and X. Zhao, *J. Energy Chem.*, 2021, **57**, 247–280.
18 S. L. Chou, Y. Pan, J. Z. Wang, H. K. Liu and S. X. Dou, *Phys. Chem. Chem. Phys.*, 2014, **16**, 20347–20359.
19 D. Bresser, D. Buchholz, A. Moretti, A. Varzi and S. Passerini, *Energy Environ. Sci.*, 2018, **11**, 3096–3127.
20 S. Nayak, G. Sahoo, I. I. Das, A. K. Mohanty, R. Kumar, L. Sahoo and J. K. Sundaray, *Toxics*, 2023, **11**(6), 543.
21 X. Lim, *Nature*, 2023, **620**, 24–27.
22 Y. Zhang and M. Naebe, *ACS Sustain. Chem. Eng.*, 2021, **9**, 1427–1442.
23 W. J. Chen, C. X. Zhao, B. Q. Li, T. Q. Yuan and Q. Zhang, *Green Chem.*, 2022, **24**, 565–584.
24 A. Beaucamp, M. Muddasar, I. S. Amiinu, M. Moraes Leite, M. Culebras, K. Latha, M. C. Gutiérrez, D. Rodriguez-Padron, F. del Monte, T. Kennedy, K. M. Ryan, R. Luque, M. M. Titirici and M. N. Collins, *Green Chem.*, 2022, **24**, 8193–8226.
25 J. M. Yuan, W. F. Ren, K. Wang, T. T. Su, G. J. Jiao, C. Y. Shao, L. P. Xiao and R. C. Sun, *ACS Sustain. Chem. Eng.*, 2022, **10**, 166–176.
26 H. Lu, A. Cornell, F. Alvarado, M. Behm, S. Leijonmarck, J. Li, P. Tomani and G. Lindbergh, *Materials*, 2016, **9**, 1–17.
27 T. Chen, Q. Zhang, J. Pan, J. Xu, Y. Liu, M. Al-Shroofy and Y. T. Cheng, *ACS Appl. Mater. Interfaces*, 2016, **8**, 32341–32348.
28 C. Luo, L. Du, W. Wu, H. Xu, G. Zhang, S. Li, C. Wang, Z. Lu and Y. Deng, *ACS Sustain. Chem. Eng.*, 2018, **6**, 12621–12629.
29 R. Gond, H. D. Asfaw, O. Hosseinaei, K. Edström, R. Younesi and A. J. Naylor, *ACS Sustain. Chem. Eng.*, 2021, **9**, 12708–12717.
30 X. Xu, K. Wang, Y. Zhou, C. Lai, D. Zhang, C. Xia and A. Pugazhendhi, *Fuel*, 2023, **338**, 127361.
31 H. Q. Lê, A. Zaitseva, J. P. Pokki, M. Ståhl, V. Alopaeus and H. Sixta, *ChemSusChem*, 2016, **9**, 2939–2947.
32 W. Fang and H. Sixta, *ChemSusChem*, 2015, **8**, 73–76.
33 A. Sluiter, R. Ruiz, C. Scarlata, J. Sluiter and D. Templeton, *Natl. Renew. Energy Lab.*, 2008, **9**.
34 A. Sluiter, B. Hames, R. Ruiz, C. Scarlata, J. Sluiter, D. Templeton and D. Crocker, *Natl. Renew. Energy Lab.*, 2008, **17**.
35 C. Nita, B. Zhang, J. Dentzer and C. Matei Ghimbeu, *J. Energy Chem.*, 2021, **58**, 207–218.
36 A. Beda, J. M. Le Meins, P. L. Taberna, P. Simon and C. Matei Ghimbeu, *Sustainable Mater. Technol.*, 2020, **26**, e00227.
37 C. del Mar Saavedra Rios, L. Simonin, C. M. Ghimbeu, C. Vaulot, D. da Silva Perez and C. Dupont, *Fuel Process. Technol.*, 2022, **231**, 107223.
38 D. E. Newbury and N. W. M. Ritchie, *Scanning*, 2013, **35**, 141–168.
39 A. Kamiyama, K. Kubota, T. Nakano, S. Fujimura, S. Shiraishi, H. Tsukada and S. Komaba, *ACS Appl. Energy Mater.*, 2020, **3**, 135–140.
40 V. Velez, G. Ramos-Sánchez, B. Lopez, L. Lartundo-Rojas, I. González and L. Sierra, *Carbon*, 2019, **147**, 214–226.
41 L. Sbrascini, A. Staffolani, L. Bottoni, H. Darjazi, L. Minnetti, M. Minicucci and F. Nobili, *ACS Appl. Mater. Interfaces*, 2022, **14**(29), 33257–33273.
42 D. Mp, M. Misra and A. K. Mohanty, *Environ. Sci.: Adv.*, 2023, **2**, 1282–1301.

43 M. Bartoli, A. Piovano, G. Antonio, G. Meligrana, C. Tealdi, G. Pagot, E. Negro, R. Pedraza, C. Triolo, L. Vazquez, N. Comisso, A. Tagliaferro, S. Santangelo, E. Quartarone, V. Di, P. Mustarelli, R. Ruffo and C. Gerbaldi, *Renewable Sustainable Energy Rev.*, 2024, **194**, 114304.
44 S. Puravankara and Nagmani, *ACS Appl. Energy Mater.*, 2020, **3**, 10045–10052.
45 K. Yu, X. Wang, H. Yang, Y. Bai and C. Wu, *J. Energy Chem.*, 2021, **55**, 499–508.
46 C. Matei Ghimbeu, J. Górka, V. Simone, L. Simonin, S. Martinet and C. Vix-Guterl, *Nano Energy*, 2018, **44**, 327–335.
47 J. Domínguez-Robles, T. Tamminen, T. Liitiä, M. S. Peresin, A. Rodríguez and A. S. Jääskeläinen, *Int. J. Biol. Macromol.*, 2018, **106**, 979–987.
48 Y. Li, Y. Liu, W. Chen, Q. Wang, Y. Liu, J. Li and H. Yu, *Green Chem.*, 2016, **18**, 1010–1018.
49 Z. Zhang, M. D. Harrison, D. W. Rackemann, W. O. S. Doherty and I. M. O'Hara, *Green Chem.*, 2016, **18**, 360–381.
50 R. Rinaldi, R. Jastrzebski, M. T. Clough, J. Ralph, M. Kennema, P. C. A. Bruijnincx and B. M. Weckhuysen, *Angew. Chem., Int. Ed.*, 2016, **55**, 8164–8215.
51 C. M. Hansen, *Hansen Solubility Parameters*, Taylor & Francis Group, 2nd edn, 2007.
52 X. Tan, Q. Zhang, W. Wang, X. Zhuang, Y. Deng and Z. Yuan, *Fuel*, 2019, **249**, 334–340.
53 Q. Li, Y. Dong, K. D. Hammond and C. Wan, *J. Mol. Liq.*, 2021, **344**, 117779.
54 E. Jasiukaitytė-Grojzdek, M. Huš, M. Grilc and B. Likozar, *ACS Sustain. Chem. Eng.*, 2020, **8**, 17475–17486.
55 Y. H. Xu, P. Zeng, M. F. Li, J. Bian and F. Peng, *Sep. Purif. Technol.*, 2021, **279**, 119780.
56 I. Cybulska, G. Brudecki, K. Rosentrater, J. L. Julson and H. Lei, *Bioresour. Technol.*, 2012, **118**, 30–36.
57 X. Erdocia, R. Prado, M. Á. Corcuera and J. Labidi, *J. Ind. Eng. Chem.*, 2014, **20**, 1103–1108.
58 C. Inkrod, M. Raita, V. Champreda and N. Laosiripojana, *BioEnergy Res.*, 2018, **11**, 277–290.
59 H. Yang, R. Yan, H. Chen, D. H. Lee and C. Zheng, *Fuel*, 2007, **86**, 1781–1788.
60 D. Watkins, M. Nuruddin, M. Hosur, A. Tcherbi-Narteh and S. Jeelani, *J. Mater. Res. Technol.*, 2015, **4**, 26–32.
61 K. Wang, Y. Jin, S. Sun, Y. Huang, J. Peng, J. Luo, Q. Zhang, Y. Qiu, C. Fang and J. Han, *ACS Omega*, 2017, **2**, 1687–1695.
62 N. Zhang, Q. Liu, W. Chen, M. Wan, X. Li, L. Wang, L. Xue and W. Zhang, *J. Power Sources*, 2018, **378**, 331–337.
63 F. Wang, T. Zhang and F. Ran, *Electrochim. Acta*, 2023, **441**, 141770.
64 V. Augustyn, J. Come, M. A. Lowe, J. W. Kim, P. L. Taberna, S. H. Tolbert, H. D. Abruña, P. Simon and B. Dunn, *Nat. Mater.*, 2013, **12**, 518–522.
65 Y. Liu, H. Dai, L. Wu, W. Zhou, L. He, W. Wang, W. Yan, Q. Huang, L. Fu and Y. Wu, *Adv. Energy Mater.*, 2019, **9**, 1–9.
66 Y. Wan, Y. Liu, D. Chao, W. Li and D. Zhao, *Nanomater. Sci.*, 2022, **5**, 189–201.
67 C. Chen, Y. Huang, Y. Zhu, Z. Zhang, Z. Guang, Z. Meng and P. Liu, *ACS Sustain. Chem. Eng.*, 2020, **8**, 1497–1506.
68 W. Li, X. Guo, K. Song, J. Chen, J. Zhang, G. Tang, C. Liu, W. Chen and C. Shen, *Adv. Energy Mater.*, 2023, **13**, 1–10.
69 L. Minnetti, F. M. Maddar, A. K. Haridas, M. Capener, F. Nobili and I. Hasa, *Batteries Supercaps*, 2025, **8**, e202400645.
70 H. Darjazi, L. Bottoni, H. R. Moazami, S. J. Rezvani, L. Balducci and L. Sbrascini, *Mater. Today Sustain.*, 2023, 100313.
71 H. Chen, M. Ling, L. Hencz, H. Y. Ling, G. Li, Z. Lin, G. Liu and S. Zhang, *Chem. Rev.*, 2018, **118**, 8936–8982.
72 A. Staffolani, L. Sbrascini, L. Bottoni, L. Minnetti, H. Darjazi, A. Trapananti and F. Paparoni, *Energy Adv.*, 2024, **3**, 1726.
73 L. Minnetti, L. Sbrascini, A. Staffolani, V. Marangon, F. Nobili and J. Hassoun, *J. Energy Chem.*, 2024, **96**, 300–317.